quantum beam science

MDPI

Article

Metallic Ca Aggregates Formed Along Ion Tracks and Optical Anisotropy in CaF_2 Crystals Irradiated with Swift Heavy Ions

Hiroshi Amekura [1,*], Norito Ishikawa [2], Nariaki Okubo [2], Feng Chen [3], Kazumasa Narumi [4], Atsuya Chiba [4], Yoshimi Hirano [4], Keisuke Yamada [4], Shunya Yamamoto [4] and Yuichi Saitoh [5]

1 National Institute for Materials Science (NIMS), Tsukuba 305-0003, Ibaraki, Japan
2 Japan Atomic Energy Agency (JAEA), Tokai 319-1195, Ibaraki, Japan; ishikawa.norito@jaea.go.jp (N.I.); okubo.nariaki@jaea.go.jp (N.O.)
3 School of Physics, Shandong University, Jinan 250100, China; drfchen@sdu.edu.cn
4 National Institutes for Quantum Science and Technology (QST), Takasaki 370-1292, Gunma, Japan; narumi.kazumasa@qst.go.jp (K.N.); chiba.atsuya@qst.go.jp (A.C.); hirano.yoshimi@qst.go.jp (Y.H.); yamada.keisuke@qst.go.jp (K.Y.); yamamoto.shunya@qst.go.jp (S.Y.)
5 National Institutes for Quantum Science and Technology (QST), Inage 263-8555, Chiba, Japan; saito.yuichi@qst.go.jp
* Correspondence: amekura.hiroshi@nims.go.jp; Tel.: +81-29-863-5479

Abstract: It is known that swift heavy ion (SHI) irradiation induces the shape elongation of metal nanoparticles (NPs) embedded in transparent insulators, which results in anisotropic optical absorption. Here, we report another type of the optical anisotropy induced in CaF_2 crystals without including intentionally embedded metal NPs. The CaF_2 samples were irradiated with 200 MeV Xe^{14+} ions with an incident angle of 45° from the surface normal. With the increasing fluence, an absorption band at ~550 nm, which is ascribed to Ca aggregates, increases both the intensity and the anisotropy. XTEM observation clarified the formation of the continuous line structures and the discontinuous NP chains parallel to the SHI beam. Numerical simulations of the optical absorption spectra suggested the NP chains but not the continuous line structures as the origin of the anisotropy. The optical anisotropy in CaF_2 irradiated with SHIs is different from the shape elongation of NPs.

Keywords: swift heavy ion; CaF_2; anisotropic optical absorption; nanoparticles; metal aggregate

Citation: Amekura, H.; Ishikawa, N.; Okubo, N.; Chen, F.; Narumi, K.; Chiba, A.; Hirano, Y.; Yamada, K.; Yamamoto, S.; Saitoh, Y. Metallic Ca Aggregates Formed Along Ion Tracks and Optical Anisotropy in CaF_2 Crystals Irradiated with Swift Heavy Ions. *Quantum Beam Sci.* **2024**, *8*, 29. https://doi.org/10.3390/qubs8040029

Academic Editors: Klaus-Dieter Liss and David Cohen

Received: 19 August 2024
Revised: 20 September 2024
Accepted: 31 October 2024
Published: 7 November 2024

1. Introduction

A huge number of studies have already been devoted to surface plasmon resonances (SPRs) of metal nanoparticles (NPs) embedded in transparent insulators because these metal NPs show much faster optical responses than semiconductors due to the electric field enhancement in nanometric regions, etc. [1]. To add further functionality to NPs, it is more attractive if the SPR can be controlled by the polarization angles of polarized light: e.g., while the *s*-polarized light excites the SPR, the *p*-polarized light of the same frequency does not. This can be easily attained if non-spherical nanoparticles (NPs) can be prepared. For example, triple-degenerated SPR in a spherical NP is divided into a double-degenerated transverse SPR and a single-degenerated longitudinal SPR in a spheroidal NP. However, to gain enough signal intensity for certain applications, elongation axes of many spheroidal NPs should be aligned in parallel with each other.

In this respect, an attractive phenomenon, called "shape elongation of embedded NPs", is known, induced by swift heavy ion (SHI) irradiation [2–4]. SHIs are extremely high-energy ions, e.g., higher than several tens of MeV, where the nuclear energy loss S_n is negligible compared to the electronic energy loss S_e [5]. Under SHI irradiation, metal NPs embedded in certain matrices, e.g., silica glass (SiO_2), show shape elongation along the SHI beam direction. Therefore, all the NPs which fulfill the elongation conditions [3,4] show shape elongation toward the same direction. Because of the (quasi)conservation

of NP volume [3,4], the dimensions of NPs perpendicular to the SHI beam show shape shrinkage. (Although the mechanism must be different, non-spherical Cu NPs were formed in $MgAl_2O_4$ under 60 keV Cu implantation [6].)

While the recent major consensus on the elongation mechanism is the movement of molten metal through low-density track cores of the matrix [4,7], the ion-hammering (IH) mechanism was believed for long time before then. If IH was involved in the mechanism, the elongation of NPs could be induced in amorphous matrices only, because IH is basically induced in amorphous materials only.

While the shape elongation phenomena were confirmed in more than ten metal species of NPs [3,4], the species of the matrices are very few and mostly limited to amorphous materials such as amorphous SiO_2 [2], amorphous Si_3N_4 [8], amorphous $LiNbO_3$ [9], and amorphous $Y_3Al_5O_{12}$ (YAG) [10]. One of the reasons why the amorphous matrices were used is inevitable: SHI irradiation induces the elongation of NPs, simultaneously transforming certain crystalline materials to amorphous ones. Furthermore, NPs are often formed in the matrices by ion implantation, which often induces the amorphization of the matrices.

In this context, we have prepared Au NPs on the surface of silica glass, which were then embedded by three different matrices, i.e., $In_{1-x}Sn_xO_y$ (ITO, x ~ 0.1), amorphous carbon (a-C), and CaF_2 [11]. First, Au NPs were prepared on silica substrates by electron beam deposition of a 3 nm-thick Au film and subsequent rapid thermal annealing. Then, the Au NPs were covered by the three different matrices of approximately 50 nm thick using magnetron sputtering (ITO and CaF_2) and arc deposition (a-C). The Au NPs, half of which were embedded with three different matrices and the other with SiO_2, were irradiated with SHIs of 200 MeV Xe.

ITO half-embedding of Au NPs exhibited an XRD peak of ITO even after the SHI irradiation to a high fluence of 2×10^{14} ions/cm^2, indicating that the crystallinity was maintained. At the same fluences, the Au NPs half-embedded in ITO exhibit more efficient shape elongation than those fully embedded in silica. Therefore, this observation strongly confirmed that the shape elongation of NPs is induced even in a crystalline matrix [11]. In contrast, Au NPs half-embedded in a-C showed minimal elongation. While the NPs showed quite weak elongation on the silica side, they showed almost no elongation on the a-C side. This observation indicated that no elongation was induced even in an amorphous matrix [11].

The results of the NPs half-embedded in CaF_2 showed loss of reproducibility. In fact, the CaF_2 films showed a very strong purple color due to defects, although they are relatively thin at around ~50 nm, indicating quite poor crystallinity [11]. In fact, point defects are introduced in CaF_2 under various irradiations, including electrons [12], protons [13], SHIs [14–16], and even X-rays [17]. According to Ref. [18], the primary process of the point defect formation in CaF_2 is the formation of so-called Frenkel pairs in halides, i.e., F- and H-centers. Particularly, F-centers aggregate with each other and form large F_n-centers, which transform to Ca collides. Concerning the shape elongation phenomenon of embedded metal NPs, changes in the matrix material induced by SHI irradiation, through the point defect formation, have been neglected or at least not considered.

In this paper, Ag NPs in CaF_2 were prepared using a different method from Ref. [11], i.e., Ag ion implantation on CaF_2 single crystals. The formation of Ag NPs in CaF_2 was confirmed by the observation of SPR of Ag NPs. Furthermore, the shape elongation of NPs was confirmed as the observation of the anisotropic optical absorption, i.e., the optical absorption depending on the polarization angle of the incident light. Since we have already succeeded in forming elongated Ag NPs in YAG crystals by the same procedures, i.e., 200 keV Ag ion implantation and 200 MeV Xe irradiation, the formation of Ag NPs and the elongation in CaF_2 have been rigidly confirmed because we have experienced that Ag NPs showed quite similar spectra, irrespective of the different matrices, i.e., CaF_2 and YAG [10].

One of the most important observations in Ag NPs in CaF_2 is that a new peak around 550 nm appeared and the intensity increased under SHI irradiation. The peak was also

observed in CaF_2 samples without Ag NPs under SHI irradiation, which exhibited optical anisotropy. This paper describes the observation of the newly observed peak with the anisotropy, corresponding transmission electron microscopy (TEM) images, and numerical simulations of the optical spectra.

2. Materials and Methods

Calcium fluoride (CaF_2) has a crystalline structure of the fluorite type, i.e., in the cubic symmetry. Single crystals of CaF_2 with sizes of 10 × 10 × 1 mm^3 were purchased from ATOM Optics Co., Ltd., Shanghai, China. The largest surface of 10 mm × 10 mm corresponded to the (001) crystalline plane. Some pieces of the CaF_2 crystals were implanted with 200 keV Ag^+ ions from a 400 kV ion implanter in Takasaki Institute for Quantum Science and Technology, QST. An incident angle of 5° from the surface normal was applied to avoid channeling implantation. The ion range and straggling of 200 keV Ag ions in CaF_2 in an off-axis implantation were calculated by SRIM 2013 [19] as 75.9 nm and 23.1 nm, respectively. Samples were implanted through a 7 mm × 7 mm squared aperture with the beam scanning frequencies of 89 Hz (horizontal) and 502 Hz (vertical). The implanted Ag contents for different samples were evaluated by Rutherford backscattering spectrometry (RBS) with 2 MeV He^+ ions [20]. The mean value and the standard deviation were $(1.02 \pm 0.15) \times 10^{17}$ ions/cm^2. While as-implanted samples had already shown an SPR peak, which indicated the formation of Ag NPs, post-implantation annealing was performed in a vacuum (~5 × 10^{-6} Torr) at 800 °C for 30 min to minimize the damage.

Both the pre-Ag-implanted and virgin CaF_2 samples were irradiated with SHIs of 200 MeV $^{136}Xe^{14+}$ ions from the 20 MV tandem accelerator at the Tokai Research and Development Center, JAEA. The fluence ranged from 1 × 10^{11} to 2 × 10^{14} ions/cm^2. The (001) face of the CaF_2 samples were irradiated with an ion incidence angle of 45° from the surface normal in order to evaluate the anisotropic optical absorption spectra using linearly polarized light [21]. Here, the light polarizations of 0° and 90° are those parallel and perpendicular to the ion-penetrating plane, respectively, as shown in Figure 1. The stopping powers and the projected ranges of the 200 MeV Xe ions in CaF_2 were calculated using SRIM 2013 code [19] and shown in Table 1. The Xe ion provides the electronic stopping powers S_e of 20.3 keV/nm in CaF_2, which was much higher than the track formation threshold of 5 keV/nm in CaF_2 [22], indicating the formation of ion tracks in the present samples.

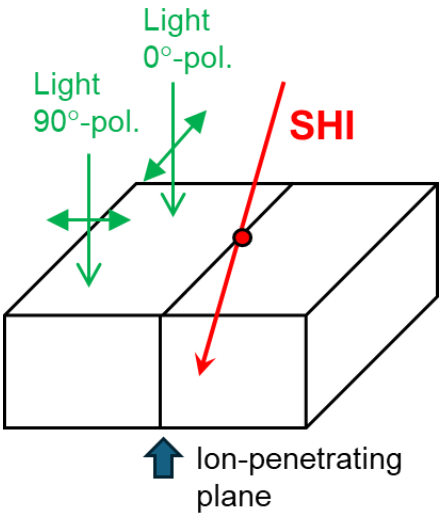

Figure 1. Schematically depicted definitions of the ion-penetrating plane and of the 0° and 90°polarization of incident lights. (Each pair of triangles indicates the direction of the polarization.) While SHIs are incident to the sample surface with an angle of 45°, light for the absorption measurements is incident normal to the surface.

Table 1. Electronic and nuclear stopping powers at the surface and the projected range of 200 MeV ^{136}Xe ions in a CaF_2 crystal, calculated by SRIM 2013 [19].

200 MeV ^{136}Xe Ions in CaF_2 Crystal:	
Electronic stopping power at the surface S_e (keV/nm)	20.3
Track formation threshold $S_{e,th}$ (keV/nm) [22]	5
Nuclear stopping power at the surface S_n (keV/nm)	0.069
Projected range R_p(μm)	16.7
Ion velocity E/m (MeV/u)	1.47

A dual-beam spectrophotometer was used for the anisotropic absorption measurements [21] in the wavelength region of 215–800 nm, with a resolution of 1 nm at room temperature. An optical polarizer (extinction ratio $< 5 \times 10^{-5}$ in this wavelength region) was inserted in front of the sample. The results were shown in the form of optical density ($-\log_{10} T$) without correction for reflection, where T denotes the optical transmittance. Cross-sectional transmission electron microscopy (XTEM) was applied using JEM-2100, JEOL, under an operation voltage of 200 kV. XTEM specimens were thinned down parallel to the ion-penetrating plane using a 30 keV Ga focused ion beam (FIB) after deposition of protective carbon layers.

3. Results

3.1. Anisotropic Optical Absorption

Figure 2a exhibits the optical density spectra detected by linearly polarized light of CaF_2 crystals including Ag NPs irradiated with 200 MeV Xe^{14+} ions to a fluence ranging from 0 to 2×10^{14} ions/cm^2. The optical density is defined as $-\mathrm{Log}_{10}\, T$, where T denotes the optical transmittance. The optical density is a quantity similar to the optical absorption but does not include a change in the optical reflectance. Solid and broken curves indicate the spectra measured with linearly polarized light with the polarizations of 0° and 90°, i.e., parallel and perpendicular to the ion-penetrating plane, respectively, as shown in Figure 1. The spectra at different fluences are vertically shifted from each other for clarity.

In an unirradiated state, a prominent peak was observed at ~420 nm, whose spectral shape did not depend on the polarization angle. Compared with literature data on the SPR peaks of Ag NPs in silica [23,24] and YAG [10], this peak is ascribed to the SPR of Ag NPs in CaF_2. A rise in the optical density below 320 nm is also characteristic of the Ag NPs [23,24]. While both the polarization curves at 0° and 90° fell on the same curve at the fluence of 1×10^{11} ions/cm^2, a small deviation was observed between them at 1×10^{12} ions/cm^2. Increasing the fluence further, the deviation between the curves at the two polarizations increased. The SPR peaks at the 0° and 90° polarizations moved to 430 nm and 400 nm, respectively, at the fluence of 5×10^{13} ions/cm^2, while both the peaks were at 420 nm in the unirradiated state. The lower (higher) energy shift of the 0° (90°) peak, i.e., the conservation of the center-of-mass of the spectra, is reasonable, because the Ag NPs elongated in the ion-penetrating plane (0°) and shrank outside of the plane (90°) [10,23,24].

It should be noted again that we, in a previous paper [11], deposited CaF_2 films over Au NPs by magnetron sputtering and irradiated them with SHIs. However, probably due to the considerably low quality of the films, we were not able to judge whether NPs were elongated in CaF_2 or not. Here, we report that Ag NPs are elongated in CaF_2 by SHI irradiation, although CaF_2 could be (partially) amorphized by the 200 keV Ag implantation.

Increasing the fluence up to 5×10^{13} ions/cm^2, the SPR peaks did not move significantly and stayed around 420 nm, except for small shifts of less than 20 nm. At 2×10^{14} ions/cm^2, the peaks largely moved to ~550 nm. However, looking carefully at the 90° curves, small changes had already begun at lower the fluences. A shoulder was observed at ~550 nm at the fluences between 1×10^{12} and 5×10^{13} ions/cm^2, although no shoulder was observed at 1×10^{11} ions/cm^2.

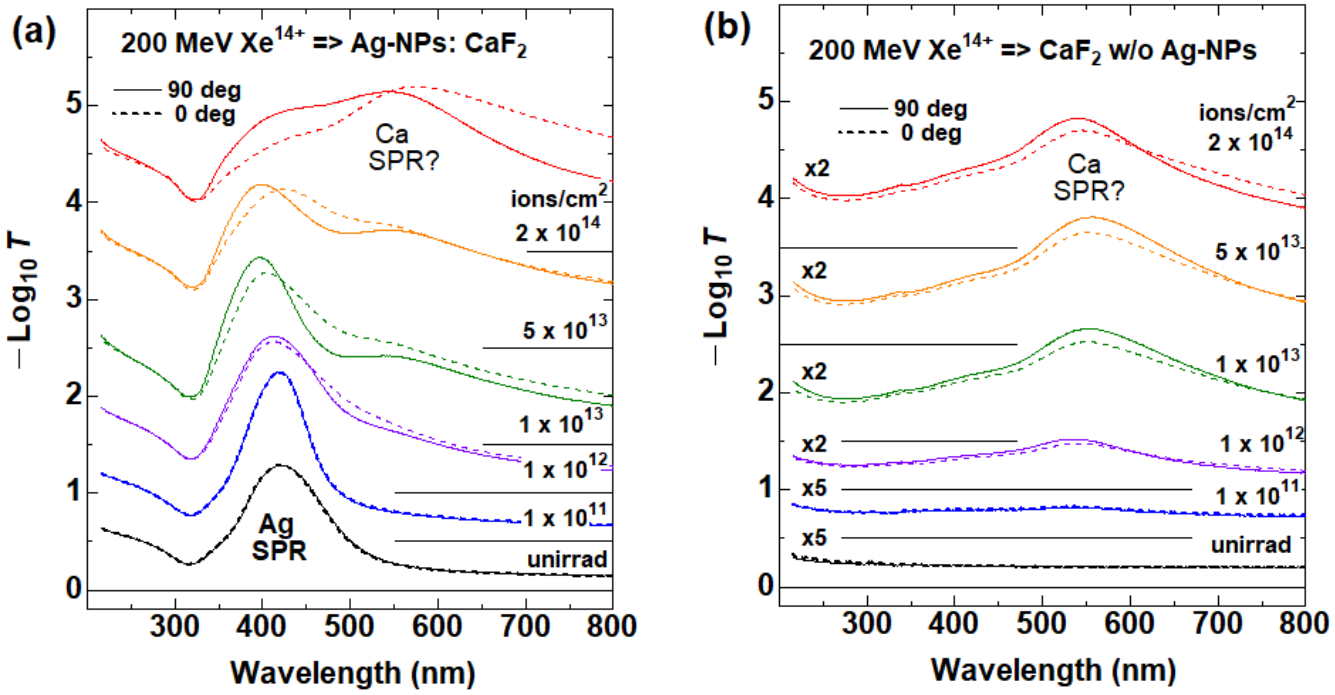

Figure 2. Optical density ($-\mathrm{Log}_{10}\,T$) spectra of CaF_2 crystals (**a**) with and (**b**) without embedded Ag nanoparticles, both irradiated with 200 MeV $^{136}Xe^{14+}$ ions at an incident angle of 45° from the surface normal, where T denotes the optical transmittance. The fluences ranged from 0 to 2×10^{14} ions/cm^2. Solid and broken curves indicate the spectra measured with linearly polarized light with a polarization angle of 0° and 90°, i.e., parallel and perpendicular to the ion-penetrating plane, respectively. The spectra at different fluences are potted in different colors and vertically shifted from each other for clarity. Horizontal lines indicate the offsets of each spectrum. Letters of ×2 and ×5 in (**b**) indicate that the spectrum is shown after expansion of two times and five times, respectively.

To collect further information, CaF_2 crystals not including Ag NPs were irradiated and evaluated in the same manner as the CaF_2 crystals including Ag NPs. The spectra are exhibited in Figure 2b. Increasing the fluence, a broad peak with the optical anisotropy appeared and grew at ~550 nm. It is known that irradiated CaF_2 crystals show two different absorption peaks: F-centers at ~380 nm and Ca aggregates at ~550 nm [13,14]. The peak observed at ~550 nm in Figure 2b can be ascribed to Ca aggregates. The F-center peak at ~380 nm is difficult to find in Figure 2b, but a very weak shoulder corresponding to the F-center was observed in our previous report [15].

It is known that Ag NPs in silica show another SPR peak at ~600 nm, when the inter-particle distances are strongly reduced [24,25]. The ~600 nm peak in silica was semi-quantitatively reproduced by the model developed by Garcia et al. who introduced the effect of the electric fields from adjacent NPs to the Maxwell–Garnett effective medium theory [26]. Therefore, the ~600 nm peak become dominant when the fluence of Ag ion implantation increases, i.e., when the inter-particle distances between Ag NPs decrease. However, as shown in Figure 2a, the ~550 nm peak increases when increasing the SHI fluence. We have no idea how to explain the decrease in the inter-particle distances with the increasing SHI fluence. In fact, Yamada et al. irradiated high-density Ag NPs, which show a ~600 nm peak, with SHIs. Since the SHI irradiation induced the shape elongation of the NPs, which resulted in an increase in the inter-particle distances, the ~600 nm peak decreased with the increasing SHI fluence. Furthermore, since the ~550 nm peak is also observed in the CaF_2 crystals not including Ag NPs, the ~550 nm peak should be ascribed to the Ca aggregates rather than the inter-particle effect of Ag NPs.

3.2. Cross-Sectional TEM Observation

While Figure 2b shows the optical density spectra of Ca aggregates, Orera and Alcala reproduced the Ca band using Mie theory [27]. While the Ca band shown in Figure 2b shows optical anisotropy, is it explained by the shape elongation of Ca aggregates? The shape elongation of NPs is efficiently induced when the diameters of the aggregates are much larger than the diameters of the ion tracks [28]. In order to judge whether Ca-aggregates are larger than the track diameters or not, and whether the shape elongation is induced in Ca aggregates or not, TEM observation was conducted.

TEM images of CaF_2 irradiated with MeV cluster ions [29] and SHIs [30] were previously reported. Figure 3a,b exhibit XTEM images of CaF_2 samples which have not been irradiated with SHIs: (a) and (b) are the images at low and medium magnification, respectively. It should be noted that Ag NPs are not included in the samples shown in Figure 3. Regions labelled by "C-layer" are carbon layers deposited on the surface of the CaF_2 samples. In the cases of irradiated samples, the "C-layers" were deposited on the irradiated surfaces. Therefore, the boundaries between the "C-layers" and the CaF_2 samples indicate the irradiated surfaces. However, this is not the case for Figure 3a,b, since they are not irradiated. The unirradiated samples (Figure 3a,b) exhibited quite rough cross-sections. Line structures were not observed, which are observed in irradiated samples.

Figure 3c–e show images of CaF_2 samples irradiated with 200 MeV Xe^{14+} ions to a fluence of 1×10^{13} ions/cm^2: both (c) and (d) are the images in medium magnification but taken at different positions, and (e) is taken with higher magnification. As shown in Figure 3c,d, huge numbers of very thin straight lines parallel to each other were observed, which extended much longer than 500 nm along the depth. The angles of the thin lines to the irradiated surface were all ~45°, which is the same as the incident angle of the SHIs. The incident angles of the SHIs are shown by arrows in Figure 3. Note that the incident angle of FIB thinning was 0° from the surface normal, which is 45° away from the direction of the thin lines. The observed straight lines are not due to the FIB thinning.

Figure 3e exhibits an expanded image of the thin lines: While the lines show continuous cylindrical shapes with a typical width of ~2.9 nm in some parts, they show discontinuous chains of NPs with a typical diameter of ~3.6 nm in other parts. At the moment, it is not known which structures, i.e., the continuous lines (shown by broken circles in Figure 3e) or the discontinuous chains (shown by solid circles), contribute to the anisotropic absorption. The structures responsible for the optical anisotropy must include Ca aggregates.

According to previous literature [31], track diameters of CaF_2 strongly depend on not only S_e but also the ion velocity. The diameters of 2.5 nm and 6 nm were extrapolated to S_e of 20 keV/nm from the data of TEM observations for the velocities of 4 MeV/u and 0.1 MeV/u, respectively. Since the 200 MeV Xe ion corresponds to S_e = 20.3 keV/nm and 1.47 MeV/u, the observed line width of 2.9 nm is comparable to the track diameter.

Figure 3f,g exhibit XTEM images at the fluences of 1×10^{12} and 5×10^{13} ions/cm^2. The density of the lines looks lower for the lower fluence (Figure 3f) and higher for the higher fluence (Figure 3g).

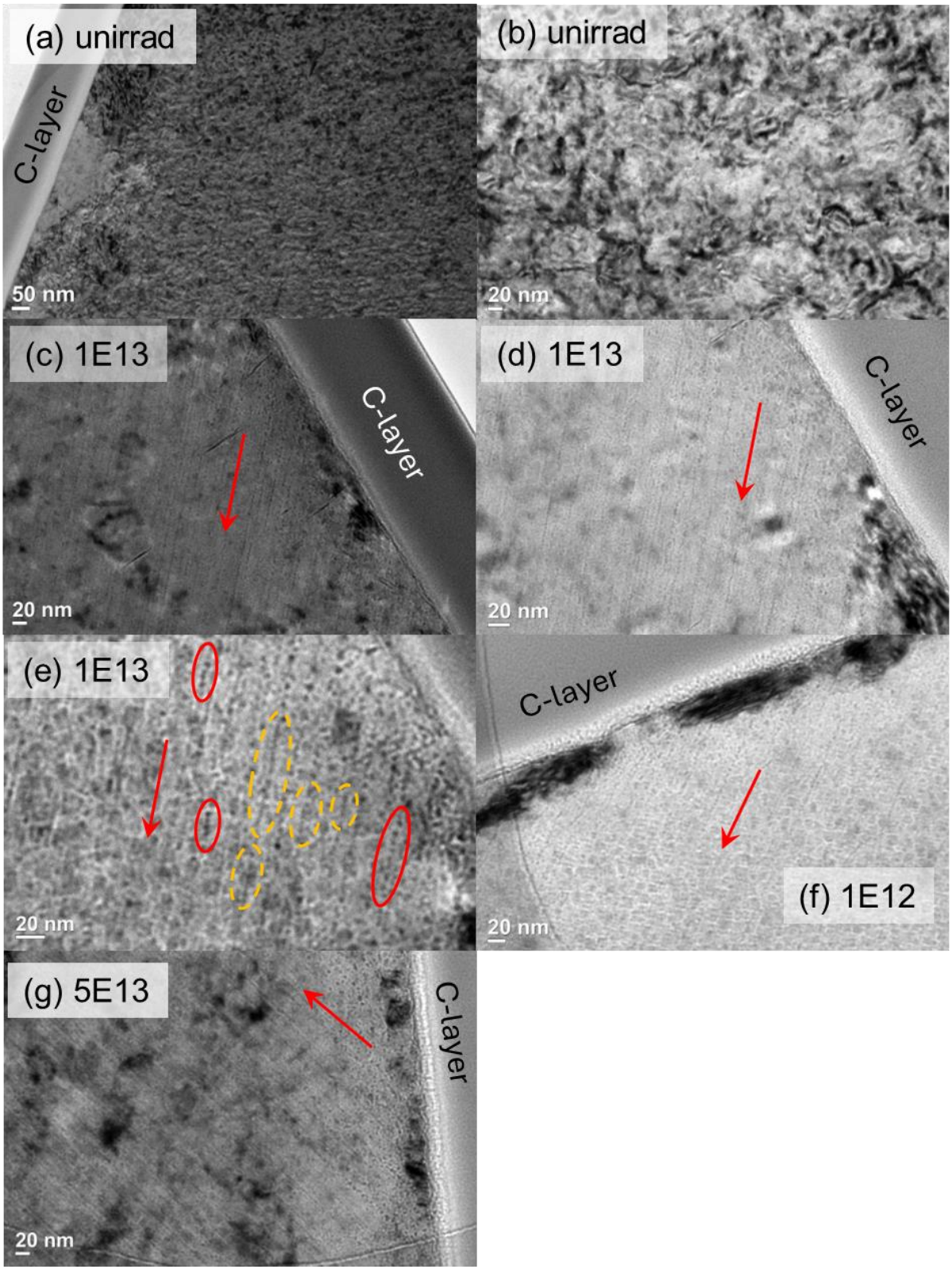

Figure 3. Cross-sectional transmission electron microscopy (XTEM) images of CaF_2 samples without Ag NPs, irradiated with 200 MeV Xe^{14+} ions to the fluence of (**a**,**b**) 0 ions/cm^2 (unirradiated), (**c**–**e**) 1×10^{13} ions/cm^2, (**f**) 1×10^{12} ions/cm^2, and (**g**) 5×10^{13} ions/cm^2. C-layer denotes carbon layers deposited on the irradiated surfaces before the FIB thinning. The incident angle of the Xe ions was 45° from the surface normal. Arrows indicate the direction of the penetrating Xe ion beams. In (**e**), examples of the NP chains and of the line structures are indicated by solid and broken circles.

4. Discussion

4.1. Possible Origins of the Optical Anisotropy

It is known that SHI irradiation of CaF_2 crystals induces the destruction of CaF_2 and the aggregation of Ca atoms as metallic Ca collide [13–15,27]. As exhibited in Figure 3, SHI irradiation formed two different structures: One was parallel straight lines which could be ascribed to the ion tracks but may contain metallic Ca. The widths of the lines are consistent with those of the ion tracks reported in previous literature [31]. The others are discontinuous NP chains aligned along the SHI beam direction.

First of all, it should be mentioned that the observed optical anisotropy in irradiated CaF_2 crystals is different from that induced by the shape elongation of embedded metallic NPs. It is known that the shape elongation of NPs is efficiently induced when the diameters of NPs are much larger than the widths of the ion tracks [28]. Since the Ca NPs observed in Figure 3e are comparable to the track diameter, large elongation is not expected [28]. The anisotropic optical absorption of CaF_2 induced with SHI irradiation shown in Figure 2b is not due to the shape elongation of NPs but to another origin. It should be noted that we have observed shape elongation of reaggregated Zn NPs which were synthesized via the decomposition of ZnO NPs under SHI irradiation [32]. However, the shape elongation is not the origin of the optical anisotropy from the CaF_2 irradiated with SHIs.

Penninkhof et al. [33] observed anisotropic optical absorption induced by SHI irradiation but not due to the shape elongation of NPs. They introduced Ag ions to BK7 glass via the ion exchange of $Ag^+ \leftrightarrow Na^+$ in a hot salt melt, and they nucleated Ag NPs up to the diameters of 2–15 nm by 1 MeV Xe irradiation. Then the sample was irradiated with 30 MeV Si ions with an incidence of 60° off-normal to a fluence of 2×10^{14} ions/cm^2. TEM observation indicated that the shape elongation of NPs was not induced but chain-like structures of NPs, which were less clear compared with those shown in Figure 3, were observed along the SHI beam. However, anisotropic absorption was detected. They reproduced the spectra using FDTD simulations, assuming a linear array of four Ag NPs [33].

As already described, the SHI irradiation formed the parallel line structures and the NP chains. An emerging question is which structures contribute the anisotropic absorption. To clarify this, optical absorption spectra of Ca nanorods (prolate spheroids) and Ca NP chains were numerically simulated and compared with the experimental spectra.

4.2. Numerical Simulations of Optical Anisotropy Spectra

Complex dielectronic functions (CDFs) of bulk Ca and CaF_2 were collected from Ref. [34] and [35], respectively. The CDF of NPs is different from that of the bulk counterpart because of the size effects. Particularly, the mean-free-path (MFP) confinement of carriers in NPs is one of the most typical size effects in metal NPs embedded in transparent insulators [1]. While the quantum size effect (QSE) is dominant in semiconductor NPs, it is negligible in metal NPs, except for very small diameters [1].

The CDF of bulk Ca is assumed to be described as a sum of the contribution of the free electrons and of the bound electrons, i.e.,

$$\varepsilon_m = \varepsilon_f + \varepsilon_b, \tag{1}$$

The former is assumed to be described as the Drude type:

$$\varepsilon_f = 1 - \frac{E_p^2}{E^2 + iE\Gamma}, \tag{2}$$

$$= 1 - \frac{\left(E_p^2/E^2\right) - i\left(E_p^2\Gamma/E^3\right)}{1 + \left(\Gamma^2/E^2\right)} \tag{3}$$

where E_p and Γ denote the plasma frequency and the carrier relaxation frequency, respectively. When $\Gamma << E$, the denominator of Equation (3) is approximated by the unity. The real and the imaginary parts of ε_f are approximated as follows:

$$\varepsilon_{f,1} = 1 - \frac{E_p^2}{E^2}, \tag{4}$$

$$\varepsilon_{f,2} = \frac{E_p^2 \Gamma}{E^3}, \tag{5}$$

The real and the imaginary parts of the CDF are plotted in Figure 4a as $(1 - \varepsilon_1)$ and $E\varepsilon_2$ versus $1/E^2$. Well-fitted linearities in both the plots confirm that the CDF of bulk Ca is well approximated by the Drude type (Equation (2)). From the slopes of curves, two quantities, E_p and Γ, were determined as 5.82 eV and 0.131 eV, respectively. Orera and Alcala reported the values of 5.78 eV and 0.018 eV from different analyses [27]. Since Γ is 0.131 eV in our case, the assumption of $\Gamma << E$ used in the derivation of Equations (4) and (5) was validated.

The carrier relaxation frequency Γ in bulk is the inverse of the carrier relaxation time, i.e., it relates to the MFP of the carriers, which is mostly limited by phonon or defect scattering in the bulk. However, in the case of NPs, the carriers are confined inside of the NPs. Therefore, the MFPs cannot be longer than the diameter of NPs. The carrier relaxation frequency $\Gamma(d)$ of NPs depends on the diameter d of NPs, which is described as follows:

$$\Gamma(d) = \Gamma_o + \frac{2V_F}{d}, \tag{6}$$

where Γ_o and V_F denote the bulk relaxation frequency and the Fermi velocity. A value of 1.28×10^8 cm/s [36] was used for V_F of Ca.

Optical absorption spectra of Ca NPs in CaF_2 crystal were calculated by the first-order Mie theory [37] using the CDF of Ca NPs (including the MFP confinement) and the CDF of CaF_2 crystal. Calculated spectra for NP diameters of 0.5, 1, 2, 3, and 5 nm are shown in Figure 4b, with comparison to an experimental spectrum. While no peak is recognized for the diameter of 0.5 nm, a peak grows when increasing the diameter to 2 nm or larger. While the calculated peak wavelength was 490 nm, the experimental one was 540 nm. The peak wavelength does not shift with the increase in diameter, as shown in Figure 4b.

The different peak wavelengths between the calculations and the experiments were explained by Orera and Alcala assuming a pressure effect on the plasmon frequency, which was exerted by the matrix. However, we present another explanation: In the experimental spectrum, a clear observation of the Ca SPR peak indicates that a high concentration of Ca atoms has aggregated, leaving a strongly damaged CaF_2 lattice. While the CDF of the perfect CaF_2 crystal was used for the calculations, the CDF of the damaged matrix may strongly change from those of the non-damaged perfect CaF_2 crystal. To simulate the change in the matrix refractive index, the absorption spectra were calculated after changing the refractive index from Δn = 0.00 to +0.25 and fixing the NP diameter to 3 nm. As shown in Figure 4c, the peak shift was reproduced around $\Delta n \sim +0.25$. The peak difference between the calculations and the experiments can be ascribed to the damage of the CaF_2 lattice.

One of the purposes of the numerical simulations of the absorption spectra is to distinguish which structures contribute to the observed anisotropic spectra, the line structures or the NP chains. Using the CDF of Ca NPs of 3 nm in diameter, i.e., Equations (2) and (6), and the bound electron contribution ε_b in Equation (1), anisotropic absorption spectra of both the structures were simulated and shown in Figure 4d. The absorption spectra of a Ca spheroid and of a pair of Ca spheres were calculated using the Rayleigh theory [38] (MQRaylgh-2.0 code [39]) and the generalized Mie theory [40] (MQAggr-1.2 code [41]), respectively. These are because the standard Mie theory is only applicable to a single spherical NP. Instead, the Rayleigh theory and the generalized Mie theory were applied to a single spheroidal NP and a pair of spherical NPs, respectively. As mentioned in Figure 4b,c,

there are discrepancies between the calculated peak wavelengths and the experimental ones. In Figure 4d, calculated spectra were plotted with the wavelength shift of +60 nm for easy comparisons with the experimental spectra.

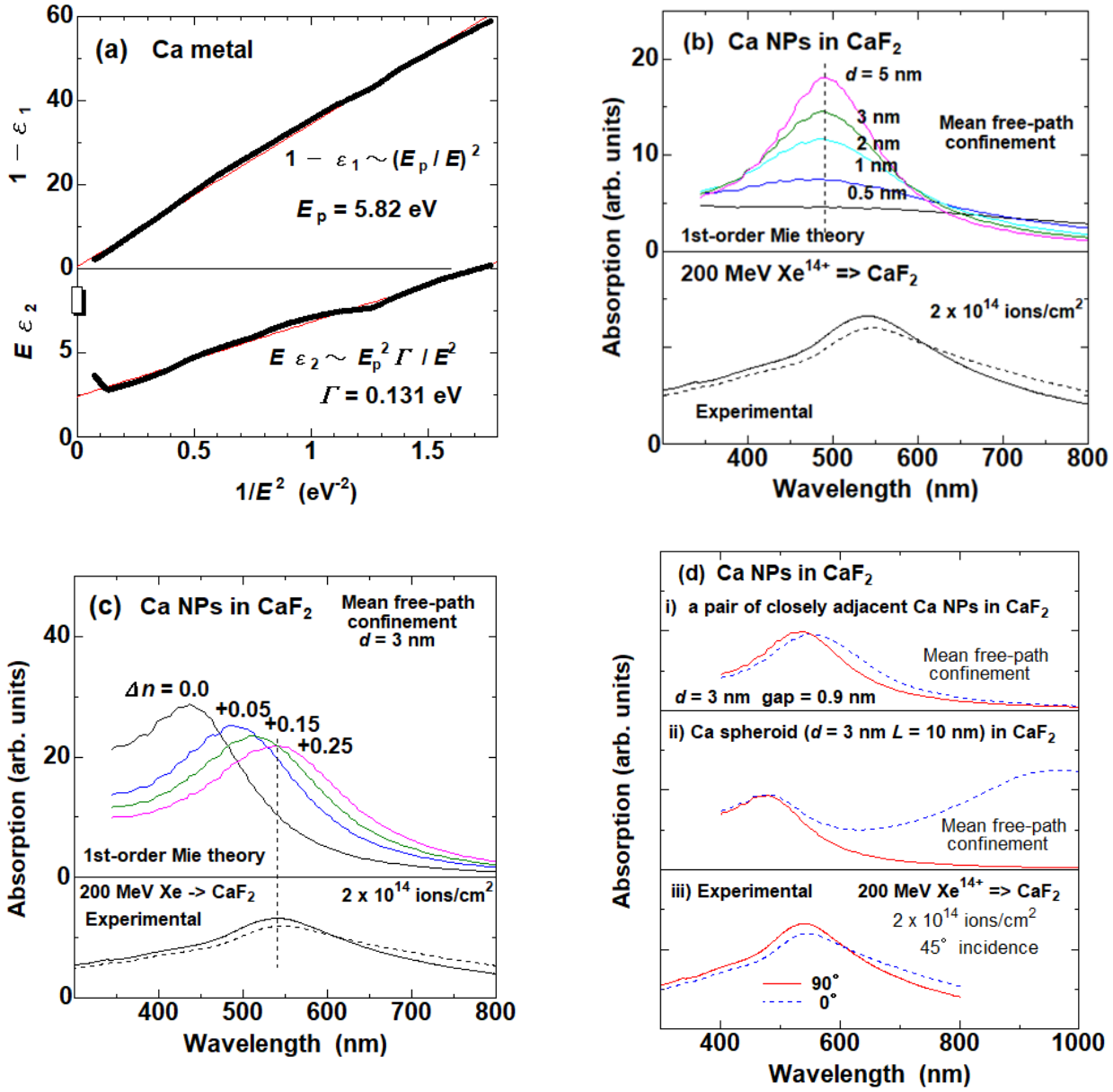

Figure 4. Comparisons of the experimental absorption spectra of an irradiated CaF_2 sample with various numerical models. (**a**) Black dots denote the real and imaginary parts of the CDFs of Ca metal from literature, which were plotted with $1/E^2$ to determine two important parameters for the Drude model, i.e., the plasma frequency E_p and the relaxation frequency Γ. Red lines show the linear fitting of the dot data by the Equations (4) and (5). Using both the parameters and the bound electrons' contribution, the absorption spectra were calculated by the 1st-order Mie theory with the MFP confinement as shown in the upper half of (**b**). The experimental spectra at 2×10^{14} ions/cm^2 are shown in the lower half. Spectra with different colors correspond to those from NPs with different diameters. In (**c**), to fit the peak wavelength, the absorption spectra were calculated with modifying the wavelength-dependent refractive index of the damaged CaF_2 matrix as $n + \Delta n$. Four spectra with different Δn between 0 and 0.25 are shown by different colors. (**d**) The experimental spectra (**iii**) were compared with two models, i.e., the Ca spheroids (**ii**) and the closely adjacent Ca NP pair (**i**). Solid and broken curves denote the spectra at 90° and 0° polarization, respectively.

The line structures were approximated by prolate spheroids [38] with a minor axis of 3 nm. While the spectra were calculated for various major axes L, only the spectra with L = 10 nm are shown in Figure 4d. While both the 0° and the 90° spectra show a peak around 475 nm, the 0° spectrum shows another peak around 1000 nm, which corresponds to a mode along the longest axis of the prolate spheroids. Since the experimental spectra are only available up to 800 nm, this is not easily determined. However, it seems that the experimental 0° spectrum does not show a considerably strong peak around 1000 nm. Hence, the spheroid model does not reproduce the experimental spectra. An analytical solution is known for the absorption spectra of an infinitely long cylinder [38,40]. The spectra were also calculated but qualitatively similar to those of a spheroid: i.e., the infinitely long cylinder model also does not reproduce the experimental spectra.

Another candidate is NP chains, which were simulated by a pair of closely adjacent spherical Ca NPs. As shown in Figure 4d, the pair of NPs reproduced the experimental spectra well in terms of the spectra's shapes, peak widths, and the degree of the anisotropy of the absorption. Here, we presumed a quite narrow gap of 0.9 nm between the two NPs in Figure 4d, because only very weak anisotropy was observed with the gap of 3 nm, and almost no anisotropy with the gap of 6 nm. The spectra of three linearly adjacent NPs were also evaluated, but the results were qualitatively similar with the pair of NPs.

Consequently, the experimental spectra were reproduced by the NP chains but not by the line structures.

5. Conclusions

Ag NPs were formed in CaF_2 single crystals by implantation of 200 keV Ag^+ ions to a fluence of 1×10^{17} ions/cm^2, and then irradiated with SHIs of 200 MeV Xe^{14+} ions to produce a fluence ranging from 0 to 2×10^{14} ions/cm^2. Anisotropic optical absorption was observed at the SPR peak of the Ag NPs, which indicated the shape elongation of Ag NPs.

In the course of the experiments, we also found that the anisotropic absorption was detected from CaF_2 crystals not including Ag NPs when irradiated with 200 MeV Xe^{14+} ions. XTEM observation clarified that a huge number of very thin straight lines of ~2.9 nm in width were formed, which can be ascribed to the ion tracks but possibly include the Ca aggregates. High-magnification observation indicated that some parts of the lines were continuous cylinders, and the other parts consisted of arrays of discontinuous Ca NPs (typically ~3.6 nm in diameter). No clear elongation of NPs was observed. The anisotropic optical absorption observed in irradiated CaF_2 is not due to the shape elongation of decomposed Ca NPs. From the comparison with the numerical simulations, the optical anisotropy is due to discontinuous but closely adjacent Ca NPs, but not to continuous Ca cylinders.

Author Contributions: Conceptualization, H.A.; sample preparation, F.C.; swift heavy ion irradiation, N.I. and N.O.; Ag ion implantation and Rutherford backscattering spectrometry, K.N., A.C., Y.H., K.Y., S.Y. and Y.S.; optical measurements and TEM observation, H.A.; writing—original draft preparation, H.A.; writing—review and editing, N.I., K.N. and H.A. All authors have read and agreed to the published version of the manuscript.

Funding: This research was funded by JSPS-KAKENHI, Grant number 22K04990. F.C. thanks support from National Natural Science Foundation of China (NSFC) under Grant No. 12235009.

Data Availability Statement: The datasets and materials generated during the current study are available from the corresponding author on reasonable request.

Acknowledgments: A part of this study was supported by the Inter-organizational Atomic Energy Research Program through an academic collaborative agreement among JAEA, QST, and the University of Tokyo. The authors are grateful to the crew of the accelerator facilities at QST-Takasaki and at JAEA-Tokai for their help. This work was supported by "Advanced Research Infrastructure for Materials and Nanotechnology in Japan (ARIM)" of the Ministry of Education, Culture, Sports, Science and Technology (MEXT). Proposal Numbers JPMXP1223NM5040 and JPMXP1224NM5073.

Conflicts of Interest: The authors declare no conflicts of interest.

References

1. Kreibig, U.; Vollmer, M. *Optical Properties of Metal Clusters*; Peter Toennies, J., Ed.; Springer: Berlin/Heidelberg, Germany, 1995; Volume 25. [CrossRef]
2. D'Orleans, C.; Stoquert, J.P.; Estournès, C.; Cerruti, C.; Grob, J.J.; Guille, J.L.; Haas, F.; Muller, D.; Richard-Plouet, M. Anisotropy of Co nanoparticles induced by swift heavy ions. *Phys. Rev. B Condens. Matter Mater. Phys.* **2003**, *67*, 220101. [CrossRef]
3. Rizza, G.; Ridgway, M.C. Ion-Shaping of Nanoparticles. In *Ion Beam Modification of Solids—Ion-Solid Interaction and Radiation Damage*; Wesch, W., Wendler, E., Eds.; Springer Series in Surface Sciences; Springer: Cham, Switzerland, 2016; Volume 61, pp. 443–473. [CrossRef]
4. Amekura, H.; Chen, F.; Jia, Y. Shape Elongation of Nanoparticles Induced by Swift Heavy Ion Irradiation. In *Ion Irradiation of Dielectrics for Photonic Applications*; Springer Series in Optical Sciences Book Series (SSOS, Volume 231); Springer Nature: Singapore, 2020; Chapter 5. [CrossRef]
5. Wesch, W.; Wendler, E. (Eds.) *Ion Beam Modification of Solids—Ion-Solid Interaction and Radiation Damage*; Springer International Publishing: Cham, Switzerland, 2016; Volume 61. [CrossRef]
6. Kiryakov, A.N.; Zatsepin, A.F.; Vagapov, A.S.; Oksengendler, B.L.; Gavrilov, N.V. Non-spherical plasmonic copper nanoparticles in a transparent $MgAl_2O_4$ ceramic matrix: Optical spectroscopy and conceptional models. *J. Phys. Chem. Solids* **2022**, *170*, 110966. [CrossRef]
7. Amekura, H.; Khan, S.A.; Kulriya, P.K.; Kabiraj, D. Irradiation Temperature Dependence of Shape Elongation of Metal Nanoparticles in Silica: Counterevidence to Ion Hammering Related Scenario. *Quantum Beam Sci.* **2023**, *7*, 12. [CrossRef]
8. Mota-Santiago, P.; Kremer, F.; Rizza, G.; Dufour, C.; Khomenkov, V.; Notthoff, C.; Hadley, A.; Kluth, P. Ion shaping of single-layer Au nanoparticles in amorphous silicon dioxide, in silicon nitride, and at their interface. *Phys. Rev. Mater.* **2020**, *4*, 096002. [CrossRef]
9. Wolf, S.; Rensberg, J.; Johannes, A.; Thomae, R.; Smit, F.; Neveling, R.; Moodley, M.; Bierschenk, T.; Rodriguez, M.; Afra, B.; et al. Shape manipulation of ion irradiated Ag nanoparticles embedded in lithium niobate. *Nanotechnology* **2016**, *27*, 145202. [CrossRef]
10. Li, R.; Pang, C.; Amekura, H.; Ren, F.; Hübner, R.; Zhou, S.; Ishikawa, N.; Okubo, N.; Chen, F. Ag nanoparticles embedded in Nd:YAG crystals irradiated with tilted beam of 200 MeV Xe ions: Optical dichroism correlated to particle reshaping. *Nanotechnology* **2018**, *29*, 424001. [CrossRef]
11. Li, R.; Narumi, K.; Chiba, A.; Hirano, Y.; Tsuya, D.; Yamamoto, S.; Saitoh, Y.; Okubo, N.; Ishikawa, N.; Pang, C.; et al. Matrix-material dependence on the elongation of embedded gold nanoparticles induced by 4 MeV C_{60} and 200 MeV Xe ion irradiation. *Nanotechnology* **2020**, *31*, 265606. [CrossRef]
12. Johnson, E.; Chadderton, L.T. Anion voidage and the void superlattice in electron irradiated CaF_2. *Radiat. EIT.* **1983**, *79*, 183–233. [CrossRef]
13. Hazem, R.; Izerrouken, M. Proton irradiation-induced defect aggregation and metallic nanoparticles in CaF_2 single-crystal. *Radiat. Phys. Chem.* **2023**, *204*, 110643. [CrossRef]
14. Boccanfuso, M.; Benyagoub, A.; Schwartz, K.; Trautmann, C.; Toulemonde, M. Study of the damage produced in CaF_2 by swift heavy ion irradiation. *Nucl. Instrum. Methods Phys. Res. Sect. B Beam Interact. Mater. At.* **2002**, *191*, 301–305. [CrossRef]
15. Amekura, H.; Li, R.; Okubo, N.; Ishikawa, N.; Chen, F. Swift heavy ion irradiation to non-amorphizable CaF_2 and amorphizable $Y_3Al_5O_{12}$ (YAG) crystals. *Nucl. Instrum. Methods Phys. Res. Sect. B Beam Interact. Mater. At.* **2020**, *474*, 78–82. [CrossRef]
16. Assylbayev, R.; Akilbekov, A.; Dauletbekova, A.; Lushchik, A.; Shablonin, E.; Vasil'chenko, E. Radiation damage caused by swift heavy ions in CaF_2 single crystals. *Radiat. Meas.* **2016**, *90*, 18–22. [CrossRef]
17. Ochs, D.; Brause, M.; Krischok, S.; Stracke, P.; Maus-Friedrichs, W.; Puchin, V.; Popov, A.; Kempter, V. Characterization of LiF and CaF_2 surfaces using MIES and UPS (HeI). *J. Electron Spectrosc. Relat. Phenom.* **1998**, *88–91*, 725–732. [CrossRef]
18. Kotomin, E.A.; Kuzovkov, V.N.; Popov, A.I. The kinetics of defect aggregation and metal colloid formation in ionic solids under irradiation. *Radiat. Eff. Defects Solids* **2001**, *155*, 113–125. [CrossRef]
19. Ziegler, J.F.; Biersack, J.P.; Ziegler, M.D. *SRIM—The Stopping and Range of Ions in Matter*; SRIM Co.: Chester, MD, USA, 2008; p. 398.
20. Doolittle, L.R. A semiautomatic algorithm for Rutherford backscattering analysis. *Nucl. Instrum. Methods Phys. Res. Sect. B Beam Interact. Mater. At.* **1986**, *15*, 227–231. [CrossRef]
21. Amekura, H.; Ishikawa, N.; Okubo, N.; Ridgway, M.C.; Giulian, R.; Mitsuishi, K.; Nakayama, Y.; Buchal, C.; Mantl, S.; Kishimoto, N. Zn nanoparticles irradiated with swift heavy ions at low fluences: Optically-detected shape elongation induced by nonoverlapping ion tracks. *Phys. Rev. B Condens. Matter Mater. Phys.* **2011**, *83*, 205401. [CrossRef]
22. Itoh, N.; Duffy, D.M.; Khakshouri, S.; Stoneham, A.M. Making tracks: Electronic excitation roles in forming swift heavy ion tracks. *J. Phys. Condens. Matter* **2009**, *21*, 474205. [CrossRef]
23. Oliver, A.; Reyes-Esqueda, J.A.; Cheang-Wong, J.C.; Roman-Velazquez, C.E.; Crespo-Sosa, A.; Rodriguez-Fernandez, L.; Seman, J.A.; Noguez, C. Controlled anisotropic deformation of Ag nanoparticles by Si ion irradiation. *Phys. Rev. B Condens. Matter Mater. Phys.* **2006**, *74*, 245425. [CrossRef]
24. Yamada, T.; Fukuda, K.; Semboshi, S.; Saitoh, Y.; Amekura, H.; Iwase, A.; Hori, F. Control of optical absorption of silica glass by Ag ion implantation and subsequent heavy ion irradiation. *Nanotechnology* **2020**, *31*, 455706. [CrossRef]
25. Liu, Z.; Wang, H.; Li, H.; Wang, X. Red shift of plasmon resonance frequency due to the interacting Ag nanoparticles embedded in single crystal SiO_2 by implantation. *Appl. Phys. Lett.* **1998**, *72*, 1823. [CrossRef]

26. García, M.A.; Llopis, J.; Paje, S.E. A simple model for evaluating the optical absorption spectrum from small Au-colloids in sol–gel films. *Chem. Phys. Lett.* **1999**, *315*, 313–320. [CrossRef]
27. Orera, V.M.; Alcalá, E. Optical properties of cation colloidal particles in CaF_2 and SrF_2. *Phys. Status Solidi* **1977**, *44*, 717–723. [CrossRef]
28. Giulian, R.; Kluth, P.; Araujo, L.L.; Sprouster, D.J.; Byrne, A.P.; Cookson, D.J.; Ridgway, M.C. Shape transformation of Pt nanoparticles induced by swift heavy-ion irradiation. *Phys. Rev. B Condens. Matter Mater. Phys.* **2008**, *78*, 125413. [CrossRef]
29. Jensen, J.; Dunlop, A.; Della-Negra, S. Microscopic observations of metallic inclusions generated along the path of MeV clusters in CaF_2. *Nucl. Instrum. Methods Phys. Res. Sect. B Beam Interact. Mater. At.* **1998**, *146*, 399–404. [CrossRef]
30. Ishikawa, N.; Taguchi, T.; Okubo, N. Hillocks created for amorphizable and non-amorphizable ceramics irradiated with swift heavy ions: TEM study. *Nanotechnology* **2017**, *28*, 445708. [CrossRef]
31. Toulemonde, M.; Benyagoub, A.; Trautmann, C.; Khalfaoui, N.; Boccanfuso, M.; Dufour, C.; Gourbilleau, F.; Grob, J.J.; Stoquert, J.P.; Costantini, J.M.; et al. Dense and nanometric electronic excitations induced by swift heavy ions in an ionic CaF_2 crystal: Evidence for two thresholds of damage creation. *Phys. Rev. B Condens. Matter Mater. Phys.* **2012**, *85*, 54112. [CrossRef]
32. Amekura, H.; Okubo, N.; Ishikawa, N.; Tsuya, D.; Mitsuishi, K.; Nakayama, Y.; Singh, U.B.; Khan, S.A.; Mohapatra, S.; Avasthi, D.K. Swift heavy ion irradiation of ZnO nanoparticles embedded in silica: Radiation-induced deoxidation and shape elongation. *Appl. Phys. Lett.* **2013**, *103*, 203106. [CrossRef]
33. Penninkhof, J.J.; Polman, A.; Sweatlock, L.A.; Maier, S.A.; Atwater, H.A.; Vredenberg, A.M.; Kooi, B.J. Mega-electron-volt ion beam induced anisotropic plasmon resonance of silver nanocrystals in glass. *Appl. Phys. Lett.* **2003**, *83*, 4137. [CrossRef]
34. Mathewson, A.G.; Myers, H.P. Absolute Values of the Optical Constants of Some Pure Metals. *Phys. Scr.* **1971**, *4*, 291. [CrossRef]
35. Daimon, M.; Masumura, A. High-accuracy measurements of the refractive index and its temperature coefficient of calcium fluoride in a wide wavelength range from 138 to 2326 nm. *Appl. Opt.* **2002**, *41*, 5275–5281. [CrossRef]
36. Kittle, C. *Introduction to Solid State Physics*, 5th ed.; John Wiley & Sons, Inc.: New York, NY, USA, 1976.
37. Mie, G. Beiträge zur Optik trüber Medien, speziell kolloidaler Metallösungen. *Ann. Phys.* **1908**, *25*, 377–445. [CrossRef]
38. Bohren, C.F.; Huffman, B.R. *Absorption and Scattering of Light by Small Particles*; John Wiley & Sons, Inc.: New York, NY, USA, 1983.
39. Quinten, M. *MQRaylgh-2.0*; Wissenschaftlich-technische Software: Aldenhoven, Germany, 2009.
40. Quinten, M. *Optical Properties of Nanoparticle Systems—Mie and Beyond*; Wiley-VCH: Weinheim, Germany, 2011. [CrossRef]
41. Quinten, M. *MQAggr-1.2*; Wissenschaftlich-Technische Software: Aldenhoven, Germany, 2012.